AIAA JOURNAL
Vol. 37, No. 3, March 1999

Limit Cycle Oscillations of a Cantilevered Wing in Low Subsonic Flow

Deman Tang,* Earl H. Dowell,† and Kenneth C. Hall‡
Duke University, Durham, North Carolina 27708-0300

A nonlinear, aeroelastic analysis of a low-aspect, rectangular wing modeled as a plate of constant thickness demonstrates that limit cycle oscillations of the order of the plate thickness are possible. The structural nonlinearity arises from double bending in both the chordwise and spanwise directions. The present results using a vortex lattice aerodynamic model for low-Mach-number flows complement earlier studies for high supersonic speed that showed similar qualitative results. Also, the theoretical results are consistent with experimental data reported by other investigators for low-aspect-ratio delta wings.

Nomenclature

a_{ij}, b_{rs}	= generalized coordinates in x, y directions
c	= plate streamwise length
D	= plate bending stiffness
E	= Young's modulus
h	= plate thickness
km, kn	= numbers of vortex elements on plate in x, y directions
kmm	= total number of vortices on both the plate and wake in x direction
L	= plate spanwise length
m	= panel mass/area, $h\rho_m$
mx, my	= numbers of structural modal functions in x, y directions defining u, v
nx, ny	= numbers of structural modal functions in x, y directions defining w
Q_{ij}	= generalized aerodynamic force
q_{mn}	= generalized coordinate in z direction
R_a	= size of reduced-order aerodynamic model
t	= time
U	= airspeed
U_f	= flutter airspeed
u, v	= in-plane displacements
w	= plate transverse deflection
$\boldsymbol{X}, \boldsymbol{Y}$	= right and left eigenvector matrices of vortex lattice eigenvalue model
x, y	= streamwise and spanwise coordinates
Z	= eigenvalue matrix of vortex lattice aerodynamic model
z	= normal coordinate
z_i	= discrete time eigenvalue
Γ	= vortex strength
Δp	= aerodynamic pressure loading on panel
$\underline{\Delta p}$	= nondimensional aerodynamic pressure, $\Delta p/(\rho_\infty U^2)$
Δt	= time step, $\Delta x/U$
Δx	= plate element length in streamwise direction
λ_i	= continuous time eigenvalues, $\ln(z_i)/\Delta t$
ν	= Poisson's ratio
ρ_∞, ρ_m	= air and plate densities
τ	= time parameter, $\sqrt{(mc^4/D)}$, s
ϕ_i, ψ_j	= transverse modal functions in x, y directions
ω	= frequencies
$\cdot$	= $\mathrm{d}(\,)/\mathrm{d}t$

Introduction

LINEAR and nonlinear aeroelastic responses of panels or plates with fixed supports on all four sides have been studied for many years. This is the so-called panel flutter phenomenon and is normally of interest with respect to individual, local skin panel oscillations on a wing or fuselage.[1] This continues to be of concern for modern aerospace vehicles such as the National Aerospace Plane.[2] Less well known is that low-aspect-ratio wings that have plate-like structural deformations can also exhibit nonlinear response including limit cycle oscillations in an overall wing motion. Hopkins and Dowell[3] and Weiliang and Dowell[4] studied the limit cycle oscillations of rectangular plates with three free edges and cantilevered from the fourth side. The panel structure was of low aspect ratio and subject to quasisteady supersonic flow over one or both surfaces, a static temperature differential between the panel and its structural support, and a static pressure differential between the upper and lower surfaces of the panel. Their results provided good physical understanding about the flutter and limit cycle oscillation characteristics for such plates in a high-Mach-number supersonic flow. In particular, they demonstrated that, even with only a single edge of a plate restrained, bending tension or geometrical nonlinearities can produce limit cycle oscillation amplitudes of the order of the plate thickness.

Following the work of Refs. 3 and 4, in the present paper we use a three-dimensional time domain vortex lattice aerodynamic model and reduced-order aerodynamic technique[5,6] to investigate the flutter and limit cycle oscillation characteristics of a low-aspect-ratio wing-panel structure at low subsonic flow speeds. Again, limit cycle oscillations are found. It is noted that these theoretical results are qualitatively consistent with the experimental results of Doggett and Soistmann,[7] who studied the flutter of low-aspect-ratio delta wings.

State-Space Equations

A schematic of the wing-plate geometry with a three-dimensional vortex lattice model of the unsteady flow is shown in Fig. 1. The aeroelastic structure/fluid state-space equations are described as follows.

Nonlinear Structural Equations

The nonlinear structural equations were derived from Hamilton's principle and Lagrange's equations based on the von Kármán plate equations[1,3,4] using the total kinetic and elastic energies and the work done by applied aerodynamic loads on the plate. Approximate modes are substituted into the energy expressions and then into Lagrange's equations to yield equations of motion for each structural modal coordinate. The results are presented as follows.

Received Jan. 10, 1998; revision received August 17, 1998; accepted for publication Oct. 26, 1998.

*Research Associate, Department of Mechanical Engineering and Materials Science.
†J. A. Jones Professor and Dean of the School of Engineering.
‡Associate Professor, Department of Mechanical Engineering and Materials Science.

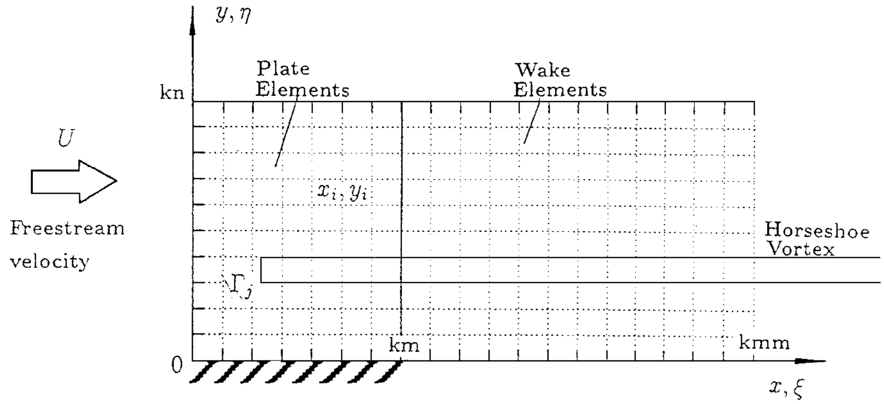

Fig. 1 Aeroelastic model of a cantilevered plate.

Structural Mode Functions and Expansions

We expand the transverse or out-of-plane displacement w and the in-plane displacements u and v as follows:

$$u = \sum_i \sum_j a_{ij}(t) u_i(x) u_j(y) \tag{1}$$

$$v = \sum_r \sum_s b_{rs}(t) v_r(x) v_s(y) \tag{2}$$

$$w = \sum_m \sum_n q_{mn}(t) \phi_m(x) \psi_n(y) \tag{3}$$

where the mode functions u_i, v_j, u_r, v_s, ϕ_m, and ψ_n are given by

$$u_i(x) = \cos i\pi(x/c), \qquad u_j(y) = \sin[(2j-1)/2]\pi(y/L)$$

$$v_r(x) = \cos r\pi(x/c), \qquad v_s(y) = \sin[(2s-1)/2]\pi(y/L)$$

$$\phi_m(x) = \sqrt{2}\sin\left[\beta_m(x/c) + \tfrac{3}{4}\pi\right] + \exp[-\beta_m(x/c)] + (-1)^{m+1}\exp\{-\beta_m[1-(x/c)]\}$$

$$\psi_n(y) = \sqrt{2}\sin\left[\beta_n(y/L) - \tfrac{1}{4}\pi\right] + \exp[-\beta_n(y/L)] + (-1)^{n+1}\exp\{-\beta_n[1-(y/L)]\} + (-1)^n\exp(-\beta_n)$$

with

$$\beta_m = \left(m - \tfrac{3}{2}\right)\pi, \qquad \beta_n = \left(n - \tfrac{1}{2}\right)\pi$$

where $\phi_m(x)$ is a free–free beam function and $\psi_n(y)$ is a cantilever beam function. For $m < 2$, the rigid-body translation and the rotation modes are

$$\phi_1(x) = 2, \qquad \phi_2(x) = 2[1 - 2(x/c)]$$

and a_{ij}, b_{rs}, q_{mn}, u, v, and w are normalized by the plate thickness h and x and y by c and L, respectively.

In-Plane Equations

It is assumed that all of the nonconservative forces act in the z direction only and the in-plane inertia may be neglected. Thus, the in-plane equations of motion are determined from the stretching strain energy and Lagrange's equation.[1,3,4] The nondimensional in-plane u and v equations are, thus,

$$\sum_k \sum_p C^{ij}_{kp} a_{kp} + \sum_g \sum_f C^{ij}_{gf} b_{gf} = C^{ij} \tag{4}$$

$$\sum_k \sum_p D^{rs}_{kp} a_{kp} + \sum_g \sum_f D^{rs}_{gf} b_{gf} = D^{rs} \tag{5}$$

where C^{ij} and D^{rs} are nonlinear (quadratic) functions of the plate transverse deflection. For details of the coefficient terms C^{ij}_{kp}, C^{ij}_{gf}, D^{rs}_{kp}, and D^{rs}_{gf} and the terms C^{ij} and D^{rs}, see Ref. 4. Note that there is a typographical error in the term C^{ij} of Ref. 4. The correct equation is

$$\begin{aligned}
C^{ij} = &-\left(\frac{h}{c}\right)^3 \sum_m \sum_n \sum_p \sum_l q_{mn} q_{pl} \\
&\times \int_0^1 \phi'_m \phi'_p u'_i \,\mathrm{d}x \int_0^1 \psi_n \psi_l v_j \,\mathrm{d}y \\
&- \nu\left(\frac{h}{L}\right)^2 \left(\frac{h}{c}\right) \sum_m \sum_n \sum_p \sum_l q_{mn} q_{pl} \\
&\times \int_0^1 \phi_m \phi_p u'_i \,\mathrm{d}x \int_0^1 \psi'_n \psi'_l v_j \,\mathrm{d}y \\
&- (1-\nu)\left(\frac{h}{L}\right)^2 \left(\frac{h}{c}\right) \sum_m \sum_n \sum_p \sum_l q_{mn} q_{pl} \\
&\times \int_0^1 \phi_m \phi'_p u'_i \,\mathrm{d}x \int_0^1 \psi'_n \psi_l v'_j \,\mathrm{d}y
\end{aligned} \tag{6}$$

Transverse Equations

The transverse equation is formed by substituting the kinetic, bending, and stretching energy expressions into Lagrange's equation. The nondimensional equation is

$$\sum_m \sum_n \left(\tau^2 A^{ij}_{mn} \ddot{q}_{mn} + B^{ij}_{mn} q_{mn}\right) + F^{ij}_N + Q^{ij} = 0 \tag{7}$$

where A^{ij}_{mn} and B^{ij}_{mn} are coefficient terms and F^{ij}_N is a nonlinear force that depends on the deflection of the plate. For details, see Ref. 4. Q^{ij} is the nondimensionalized generalized aerodynamic force. We will discuss it next.

Aerodynamic Equations: Vortex Lattice Model

The flow about the cantilever plate is assumed to be incompressible, inviscid, and irrotational. Here we use an unsteady vortex lattice method to model this flow. A typical planar vortex lattice mesh for the three-dimensional flow is shown in Fig. 1. The plate and wake are divided into a number of elements. In the wake and on the wing, all of the elements are of equal size Δx in the streamwise direction. Point vortices are placed on the plate and in the wake at the quarter chord of the elements. At the three-quarter chord of each plate element, a collocation point is placed for the downwash; i.e., we require the velocity induced by the discrete vortices to equal the downwash arising from the unsteady motion of the plate. Thus, we have the relationship

$$w_i^{t+1} = \sum_j^{kmm} K_{ij} \Gamma_j^{t+1}, \qquad i = 1, \ldots, km \tag{8}$$

where w_i^{t+1} is the downwash at the ith collocation point at time step $t+1$, Γ_j is the strength of the jth vortex, and K_{ij} is an aerodynamic kernel function.[5] As described in Ref. 5, we have three sets of equations in the wake. At the first vortex in the wake at the time step $t+1$, we have

$$\Gamma^{t+1}_{km+1} = -\sum_{j}^{km}\left(\Gamma^{t+1}_{j} - \Gamma^{t}_{j}\right) \tag{9}$$

Once the vorticity has been shed into the wake, it is convected in the wake with speed U. From the second vortex point to the last two vortex points in the wake, this convection is described numerically by

$$\Gamma^{t+1}_{i} = \Gamma^{t}_{i-1}, \qquad i = km+2, \ldots, kn-1 \tag{10}$$

At the last vortex point in the wake, we have the following relationship for the vortex distribution:

$$\Gamma^{t+1}_{i} = \Gamma^{t}_{i-1} + \alpha\Gamma^{t}_{i}, \qquad i = kn \tag{11}$$

where α is a relaxation factor; usually $0.95 < \alpha < 1.0$.

Putting together Eqs. (8–11) gives an aerodynamic matrix equation:

$$A\boldsymbol{\Gamma}^{t+1} + B\boldsymbol{\Gamma}^{t} = \boldsymbol{w}^{t+1} \tag{12}$$

where A and B are aerodynamic coefficient matrices.[5]

From the fundamental aerodynamic theory, we can obtain the pressure distribution on the plate at the jth point in terms of the vortex strengths:

$$\Delta p_j = \frac{\rho_\infty}{\Delta x}\left[U\left(\Gamma^{t+1}_{j} + \Gamma^{t}_{j}\right)/2 + \sum_{i}^{j}\Delta x\left(\Gamma^{t+1}_{i} - \Gamma^{t}_{j}\right)/\Delta t\right] \tag{13}$$

Let

$$\bar{\Gamma} \equiv \Gamma/(Uc), \qquad U \equiv \Delta x/\Delta t$$

and the overbar of Γ is then dropped for convenience. Thus, the nondimensional pressure is given by

$$\overline{\Delta p_j} = \frac{c}{\Delta x}\left[\left(\Gamma^{t+1}_{j} + \Gamma^{t}_{j}\right)/2 + \sum_{i}^{j}\left(\Gamma^{t+1}_{i} - \Gamma^{t}_{i}\right)\right] \tag{14}$$

and the aerodynamic generalized force is calculated from

$$Q^{ij} = \frac{\rho_\infty U^2 c^4}{Dh}\int_0^1\int_0^1 \overline{\Delta p}\phi_i\psi_j \,\mathrm{d}x\,\mathrm{d}y \tag{15}$$

Aeroelastic State-Space Equations

Consider a discrete-time history of the plate motion $q(t)$, with a constant sampling time step Δt. The sampled version of $q(t)$ is then defined by

$$q = \frac{(q^{t+1} + q^{t})}{2}$$

and the velocity of this discrete-time series is defined by

$$\dot{q} = \frac{(q^{t+1} - q^{t})}{\Delta t}$$

The structural dynamic equation (7) can be reconstituted as a state-space equation in discrete-time form. It is given by

$$D_2\boldsymbol{\theta}^{t+1} + D_1\boldsymbol{\theta}^{t} + C_2\boldsymbol{\Gamma}^{t+1} + C_1\boldsymbol{\Gamma}^{t} = -\boldsymbol{F}_N^{t+\frac{1}{2}} \tag{16}$$

where the vector $\boldsymbol{\theta}$ is the state of the plate, $\{\theta\} = \{\dot{q}, q\}$, and D_1 and D_2 are matrices describing the plate structural behavior. C_1 and C_2 are matrices describing the vortex element behavior on the plate itself.

There is a linear relationship between the downwash $\boldsymbol{w}$ at the collocation points and plate response $\boldsymbol{\theta}$. It is defined by

$$\boldsymbol{w} = E\boldsymbol{\theta} \tag{17}$$

Thus, combining Eqs. (12), (16), and (17), we obtain a complete aeroelastic state-space equation in matrix form:

$$\begin{bmatrix} A & -E \\ C_2 & D_2 \end{bmatrix}\begin{Bmatrix} \Gamma \\ \theta \end{Bmatrix}^{t+1} + \begin{bmatrix} B & 0 \\ C_1 & D_1 \end{bmatrix}\begin{Bmatrix} \Gamma \\ \boldsymbol{\theta} \end{Bmatrix}^{t} = \begin{Bmatrix} 0 \\ -F_N \end{Bmatrix}^{t+\frac{1}{2}} \tag{18}$$

Reduced-Order Aerodynamic Model

If we assume the structural response to be zero, then from Eq. (12) we obtain a representation of unforced fluid motion:

$$A\boldsymbol{\Gamma}^{t+1} + B\boldsymbol{\Gamma}^{t} = 0 \tag{19}$$

From Eq. (19), an aerodynamic eigenvalue problem may be formed. Because the matrices A and B are nonsymmetric, we must compute the right and left eigenvalues and eigenvectors of the generalized eigenvalue problem. They are

$$A\boldsymbol{X}Z = -B\boldsymbol{X} \tag{20}$$

and

$$A^T\boldsymbol{Y}Z = -B^T\boldsymbol{Y} \tag{21}$$

where $\boldsymbol{X}$ and $\boldsymbol{Y}$ are the right and left eigenvector matrices and Z is a diagonal matrix whose diagonal entries contain the eigenvalues. The discrete-time eigenvalues z_i are related to continuous-time eigenvalues λ_i by $z_i = \exp(\lambda_i\Delta t)$. The real part of λ_i indicates the damping of the system, and the imaginary λ_i provides the oscillation frequency.

The right and left eigenvectors are orthogonal with respect to the matrices A and B. We normalize the eigenvectors such that they are orthonormal with respect to A. Therefore,

$$\boldsymbol{Y}^T A\boldsymbol{X} = I \tag{22}$$

and

$$\boldsymbol{Y}^T B\boldsymbol{X} = -Z \tag{23}$$

Next, let the point vortex vector $\boldsymbol{\Gamma}$ be a linear combination of the R_a right eigenvectors (where in practice $R_a \ll kn \times kmm$), i.e.,

$$\boldsymbol{\Gamma} = \boldsymbol{X}_{Ra}\gamma \tag{24}$$

where $\boldsymbol{\gamma}$ is the vector of the aerodynamic modal coordinates. Substitution of Eq. (24) into Eq. (12), premultiplying Eq. (12) by $\boldsymbol{\gamma}^T_{Ra}$, and making use of the orthogonality conditions [Eqs. (22) and (23)] yields the new aeroelastic model

$$\begin{bmatrix} I & -\boldsymbol{Y}^T_{Ra}E \\ C_2\boldsymbol{X}_{Ra} & D_2 \end{bmatrix}\begin{Bmatrix} \gamma \\ \theta \end{Bmatrix}^{t+1} + \begin{bmatrix} -\boldsymbol{Z}_{Ra} & 0 \\ C_1X_{Ra} & D_1 \end{bmatrix}\begin{Bmatrix} \gamma \\ \theta \end{Bmatrix}^{t} = \begin{Bmatrix} 0 \\ -F_N \end{Bmatrix}^{t+\frac{1}{2}} \tag{25}$$

One finds that, with the reduced-order aerodynamic model, only a few aerodynamic eigenmodes need to be retained in the aeroelastic model for good accuracy. However, whereas the dominant eigenmodes have been retained, all of the eigenmodes participate in the response to some degree. To account for the neglected eigenmodes, therefore, we use a quasistatic correction, which accounts for much of their influence. This technique is similar to the mode-acceleration method common to structural dynamics and was first suggested in the context of fluid eigenmode analysis by Florea and Hall.[8] Thus, let

$$\boldsymbol{\Gamma} = \boldsymbol{\Gamma}_s + \boldsymbol{\Gamma}_d = \boldsymbol{\Gamma}_s + \boldsymbol{X}_{Ra}\gamma_d \tag{26}$$

where the first term on the right-hand side is a quasistatic solution of the vortex flow and the second term is a dynamic perturbation solution. By definition, the quasistatic portion $\boldsymbol{\Gamma}_s$ is given by

$$[A+B]\boldsymbol{\Gamma}^t_s = \boldsymbol{w}^t \tag{27}$$

where $\boldsymbol{w}^t$ is the downwash at time step t. Compare Eqs. (12) and (27). Note that Eq. (27) may be inverted once to determine $\boldsymbol{\Gamma}^t_s$ in terms of $\boldsymbol{w}^t$ and does not need to be evaluated at each time step.

Finally, the reduced-order model with static correction is given by

$$\begin{bmatrix} I & -\boldsymbol{Y}^T_{Ra}[I - A(A+B)^{-1}]E \\ C_2\boldsymbol{X}_{Ra} & D_2 + C_2(A+B)^{-1}E \end{bmatrix}\begin{Bmatrix} \gamma_d \\ \theta \end{Bmatrix}^{t+1}$$

$$+\begin{bmatrix} -Z_{Ra} & -\boldsymbol{Y}^T_{Ra}[B(A+B)^{-1}]E \\ C_1X_{Ra} & D_1 + C_1(A+B)^{-1}E \end{bmatrix}\begin{Bmatrix} \gamma_d \\ \theta \end{Bmatrix}^{t} = \begin{Bmatrix} 0 \\ -F_N \end{Bmatrix}^{t+\frac{1}{2}} \tag{28}$$

Numerical Results

Four rectangular cantilever plate models of varying aspect ratio were considered. The models are taken to be an aluminum alloy plate of constant thickness with aspect ratios of $AR \equiv L/c = 0.75$–10. The plate streamwise length $c = 0.3$ m is fixed. The plate thickness is $h = 0.001$ m, and Poisson's ratio is $\nu = 0.3$. For the basic case, the plate was modeled using 50 vortex elements, i.e., $km = 10$ and $kn = 5$. The wake was modeled using 150 vortex elements, i.e., $kmm = 40$. The total number of vortex elements (or aerodynamic degrees of freedom) is 200. The plate modal numbers are $nx = 4$, $ny = 2$, $mx = 10$, and $my = 2$. The vortex relaxation factor was taken to be $\alpha = 0.992$.

Aerodynamic Eigenmodes Analysis

Typical eigenvalues for the basic vortex lattice model are shown in Fig. 2. Figure 2a shows eigenvalues in terms of the discrete-time multiplier z, and Fig. 2b shows them in terms of the usual continuous-time eigenvalue λ. Note that for normalization purposes the airspeed U is assumed to be unity, and thus, $\Delta t = \Delta x$. It is found that there are five dominant branches in the λ distribution. (Recall that $kn = 5$.) There are 64 real and 136 complex conjugate eigenvalues.

When the wake elements are increased (note that the number of spanwise vortex locations kn does not change), the eigenvalues become denser in their distribution. A numerical example is shown in Fig. 3 for $km = 40$ and $kmm = 160$. Compare the results of Fig. 3b to those in Fig. 2b. It is seen that the eigenvalues in Fig. 2b occur again in Fig. 3b at essentially the same positions, except that the first five real eigenvalues are more heavily damped, i.e., move to the left.

To determine the contribution of the individual aerodynamic eigenmodes to the overall wing lift, a numerical experiment was considered. We assume that the wing plate is absolutely rigid and a unit step change in downwash is prescribed over the wing. The lift is defined as

$$C_L = \frac{1}{\rho_\infty U^2} \int_0^1 \int_0^1 \Delta p(x, y)\,\mathrm{d}x\,\mathrm{d}y$$

The results for C_L are shown in Fig. 4.

Figure 4 shows the magnitude of the lift created by individual aerodynamic eigenmode $C_L(i)$ vs the aerodynamic eigenmode number i. For comparison, the total lift created by all eigenmodes, $C_{L,\mathrm{total}}$, is also plotted in Fig. 4, as shown by the thick bar. We plot only 90 aerodynamic eigenmodes in Fig. 4 because beyond

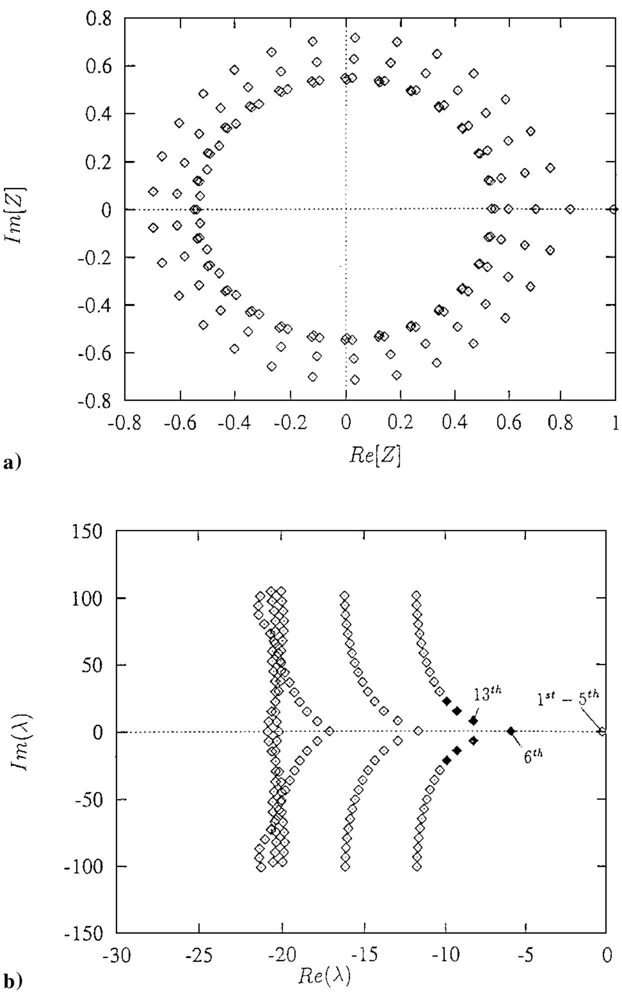

Fig. 2 Eigenvalue solutions of vortex lattice model of unsteady flow about a three-dimensional plate: $kn = 5$, $km = 10$, and $kmm = 40$; ♦, most important eigenmodes.

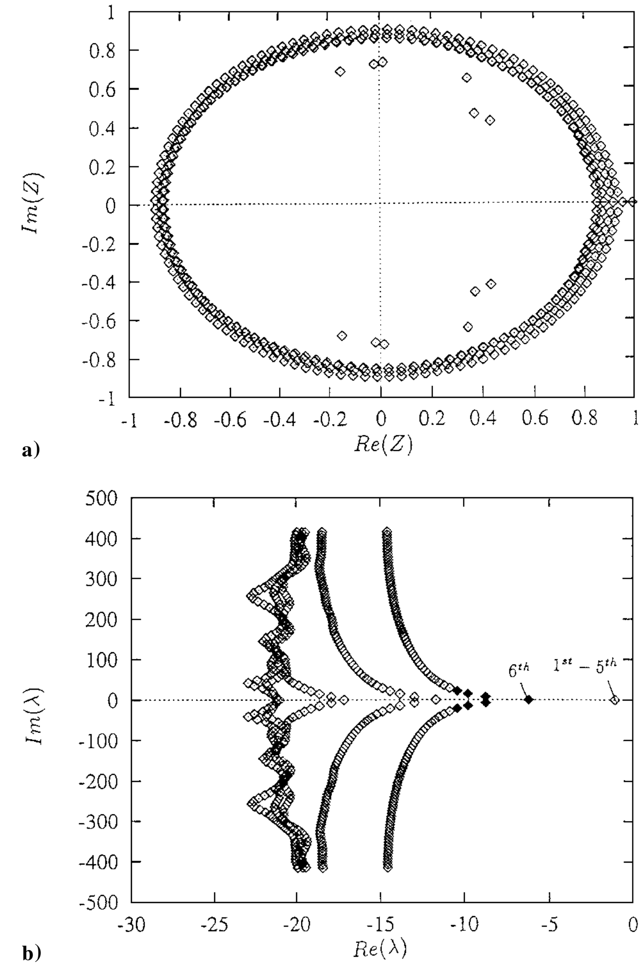

Fig. 3 Eigenvalue solutions of vortex lattice model of unsteady flow about a three-dimensional plate: $kn = 5$, $km = 40$, and $kmm = 160$.

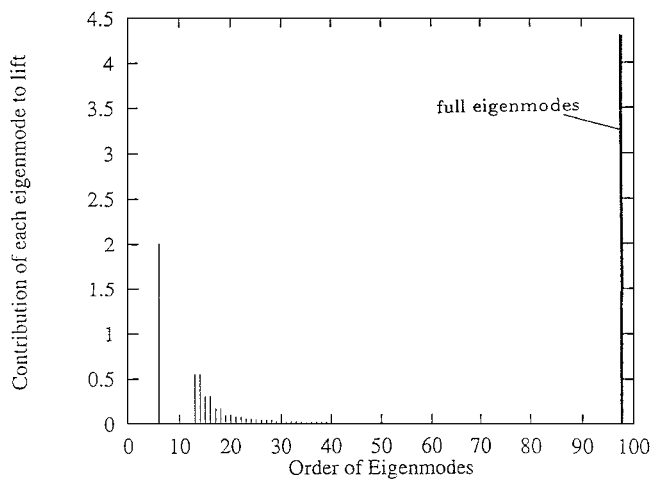

Fig. 4 Contribution of each aerodynamic eigenmode to overall wing lift.

90 eigenmodes the lift contribution is almost zero. The first 12 eigenmodes plotted are from the pure real eigenvalues, and the order is from smaller to larger damping. From the 13th eigenmode, these are the complex conjugate eigenmodes, and the order is also from smaller to larger damping. It is seen that the first important contribution is the 6th eigenmode, the second most important is from the 13th eigenmode, and the contribution decreases as the eigenmode order, i.e., damping, increases. For the pure real eigenmodes, the eigenmodes with the smallest damping are not always the most important. For example, in Fig. 2 the first five real eigenvalues are virtually identical at $\lambda_R = -0.27$ and none of them contribute significantly to the lift. In Fig. 2b, the most important eigenmodes are indicated by ♦. Thus, we find that the first λ branch is the most important. For the present example, only a few eigenmodes are significant, which provides very useful information for the flutter and nonlinear response analysis using the reduced-order aerodynamic model.

Stability of the Linear Aeroelastic Model

When the nonlinear force F_N in Eq. (18), (25), or (29) is set to zero, a linear aeroelastic model is obtained. The aeroelastic eigenvalues from solving these equations determine the stability of the system. When the real part of any one eigenvalue λ becomes positive, the entire system becomes unstable.

Figures 5a and 5b show a typical graphical representation of the eigenanalysis in the form of real eigenvalues $\mathrm{Re}(\lambda_i)$ vs the flow velocity and also a root-locus plot for the nominal linear system using all aerodynamic eigenmodes. There are two intersections of $\mathrm{Re}(\lambda_i)$ with the velocity axis. One is $U_f = 42$ m/s for the critical flutter velocity with the corresponding flutter oscillatory frequency $w_f = 76.8$ rad/s. The other is $U_d = 54.3$ m/s for the divergent velocity with zero oscillatory frequency. Note that the divergent velocity corresponds to a primarily aerodynamic mode.

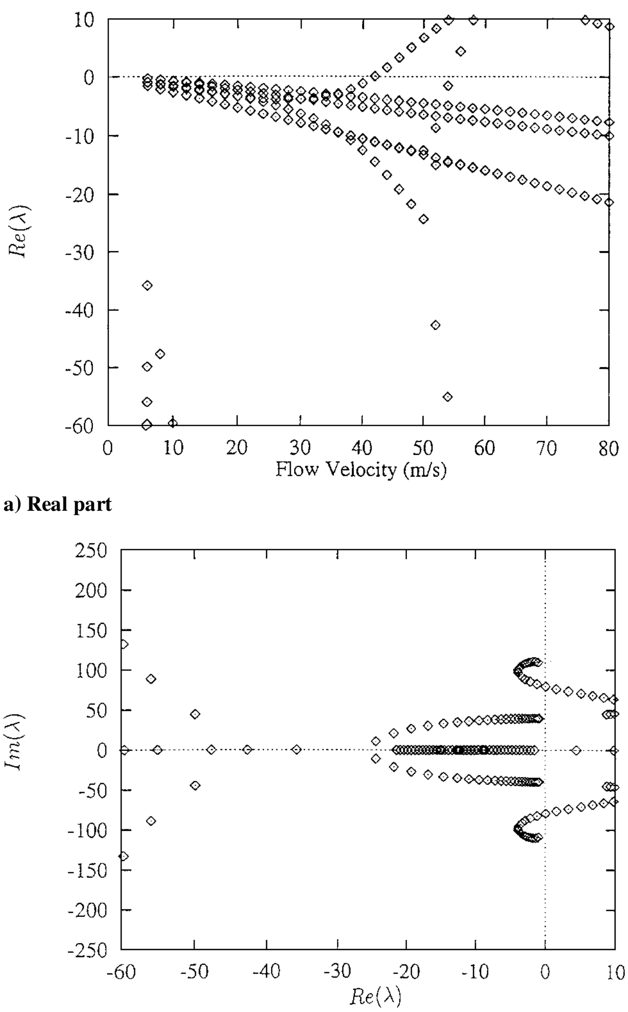

a) Real part

b) Root locus

Fig. 5 Eigenvalue solutions of linear aeroelastic model for full aerodynamic modes.

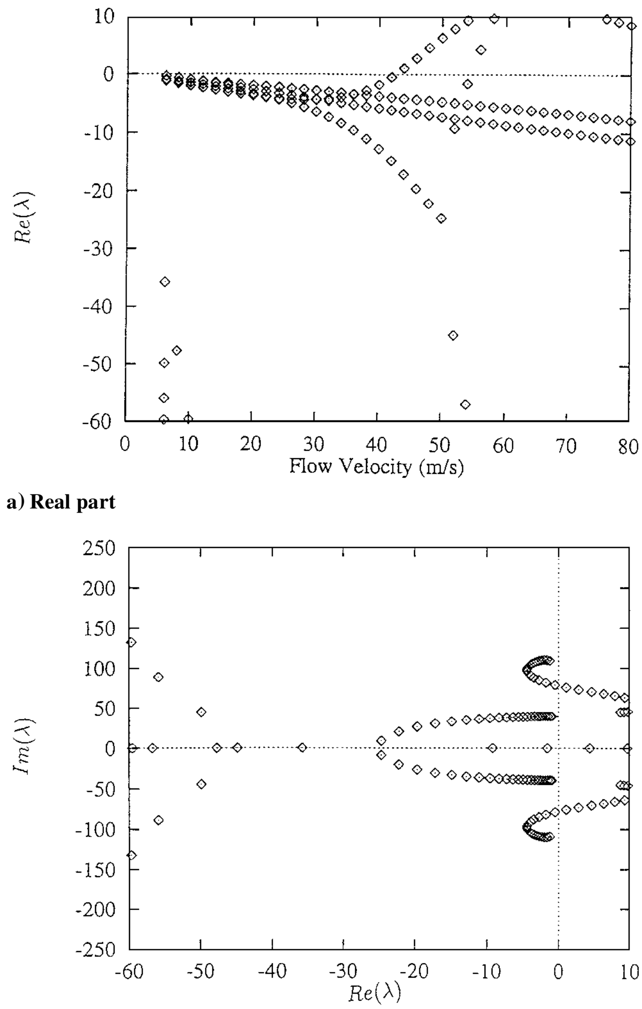

a) Real part

b) Root locus

Fig. 6 Eigenvalue solutions of linear aeroelastic model for reduced-order aerodynamic model with static correction: $R_a = 7$.

Figure 6 shows a graphical representation of the eigenanalysis using a reduced-order aerodynamic model with a static correction for seven aerodynamic eigenmodes ($R_a = 7$), i.e., the 6th and 13th–18th eigenmodes corresponding to Fig. 4. Excellent agreement between the full and reduced aerodynamic eigenmode results is obtained. However, the computation time using the reduced-order model is only about $\frac{1}{150}$ that of the original model.

From Figs. 5 and 6, it is found that the linear flutter motion is dominated by the coupling between the first two structural modes, i.e., the spanwise bending mode and the rigid plunge and rotation modes in the chordwise direction.

Figure 7 shows the flutter velocities (Fig. 7a) and flutter frequencies (Fig. 7b) of the linear system vs the aspect ratio $AR \equiv L/c$ from 0.75 to 10 using a five-eigenmode, reduced-order aerodynamic model (6th and 13th–16th) with a static correction. Both flutter velocity and corresponding frequency are increased as the aspect ratio decreases. It was found that the results for the five and seven reduced-order aerodynamic modes are virtually identical.

Figure 8 shows the convergent behavior of the linear flutter velocity vs the numbers of the structural modal function, nx and ny. Figure 8a is for the flutter velocities, and Fig. 8b is for the correspondent frequencies of the linear system. The present method has good convergence both for $ny = 1$ and $ny = 2$ when $nx > 3$. Note that the flutter velocities for $ny = 1$ are modestly higher than those for $ny = 2$. It is found that for $AR = 1$, when $ny = 1$ and $nx = 3$, the first three plate natural frequencies are 6.5, 20.5, and 71.9 Hz, whereas for $ny = 2$ and $nx = 3$, the first three plate natural frequencies are 6.5, 18.2, and 58.9 Hz. Thus, it is found that there is a lower second

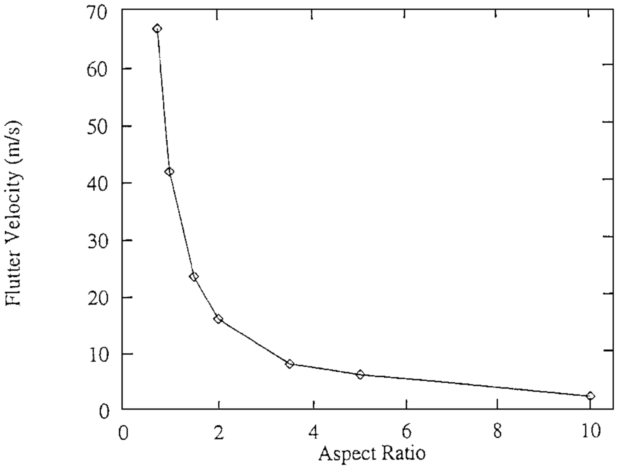

a) Flutter velocities

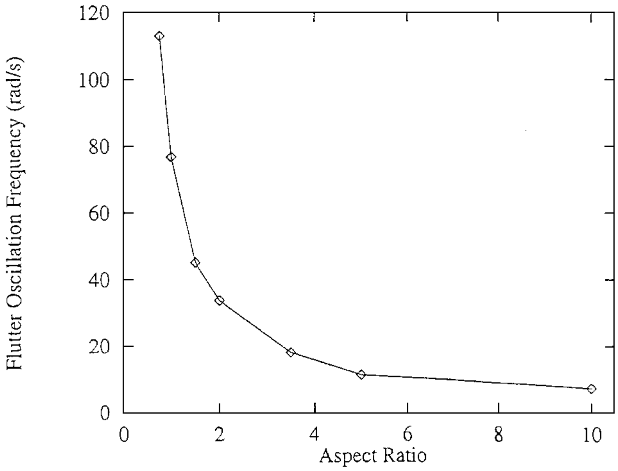

b) Oscillation frequencies

Fig. 7 Linear aeroelastic model vs aspect ratio of the plate.

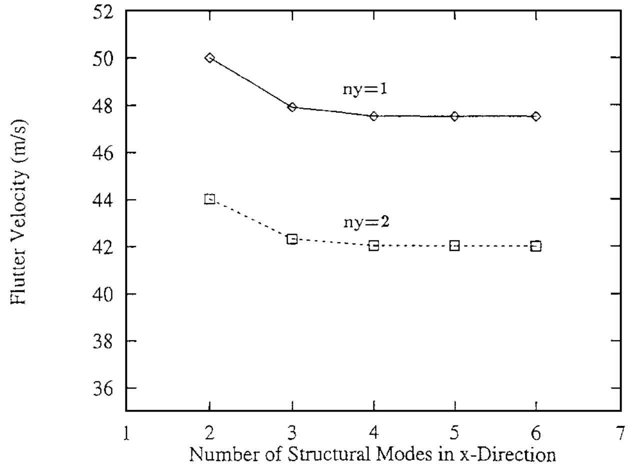

a) Flutter velocities

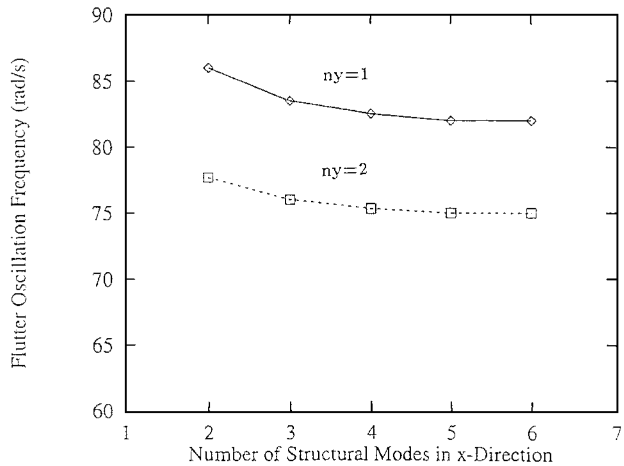

b) Oscillation frequencies

Fig. 8 Linear aeroelastic model vs the numbers of structural modal function.

natural frequency of the plate for $ny = 2$ as compared with $ny = 1$. This leads to a lower flutter velocity for $ny = 2$. The results for $ny = 3$ are essentially the same as for $ny = 2$.

Limit Cycle Oscillation of Nonlinear Model

We have used a standard discrete-time algorithm to calculate the nonlinear response of this aeroelastic system using the full aerodynamic model, Eq. (18), and also the reduced-order aerodynamic model, Eq. (28). The time step is constant for a given flow velocity U, $\Delta t = \Delta x/U$. A range of aspect ratio is considered.

Typical nondimensional transverse and in-plane displacement time histories at location ($x = 0.75$ and $y = 1$) for $U = 45$ m/s $> U_f$ are shown in Figs. 9a–9c. There is a steady-state limit cycle oscillation with frequency $\omega = 13.51$ Hz. Note that the linear flutter velocity is $U_f = 42$ m/s for $ny = 2$ and $nx = 4$. Figures 9a–9c reveal that, as the plate deflects in both the positive and negative z directions, the in-plane displacement amplitudes u and v increase in the negative x and y directions. Thus, the maximum transverse displacements w, both positive and negative, correspond to the maximum negative in-plane displacements, and the in-plane displacements oscillate at twice the transverse oscillation frequency, $\omega = 27.02$ Hz. The point at which the in-plane x displacement is at its smallest amplitude coincides with the point at which the transverse displacement is at its smallest amplitude. For a flow velocity lower than the linear flutter velocity, for example, $U = 40$ m/s, the response decays to zero, as shown in Fig. 10. Note that, if we were to change the sign of the initial conditions, then Fig. 9a would undergo a sign reversal, but Figs. 9b and 9c would be unchanged because u, $v \sim w^2$.

Comparisons of results from the full aerodynamic model with those from the reduced-order model with static correction ($R_a = 7$) have been made. Figure 11 shows a nondimensional transverse displacement time history at a certain wing location ($x = 0.75$ and $y = 1$) for $U = 45$ m/s. The solid line indicates the results from all aerodynamic eigenmodes, and the dashed line indicates results from the reduced-order aerodynamic model. The agreement is good, except that there is a slight difference in the oscillation frequency. There is also a small difference in phase from cycle to cycle that accumulates over many cycles. This is of no importance for the limit cycle itself. For transient motions, the phase is of significance, and here the differences are again small.

Figure 12 shows the nondimensional transverse peak amplitude of the limit cycle oscillation (LCO) vs the flow velocity for $AR \equiv L/c = 1$, $ny = 1$, $nx = 3$, $ny = 2$, $nx = 4$, and $ny = 2$ and $nx = 6$ for the same initial conditions, $w(0)(x = 1,\ y = 1) = 0.1$. The solid line indicates the results from the full aerodynamic eigenmode model, and the dashed line indicates results from the reduced-order aerodynamic model with $R_a = 7$. The results again show good agreement between the two aerodynamic models. From Fig. 12, it is seen that the results of one mode along the span direction ($ny = 1$) combined with three modes along the flow direction ($nx = 3$) are somewhat different from those for $ny = 2$ and $nx = 4$ and $ny = 2$ and $nx = 6$. The latter results are well converged, as suggested by the earlier results from linear theory (see Fig. 8). Figure 13 shows the oscillation frequency of the LCO vs the flow velocity for $AR \equiv L/c = 1$ and $ny = 2$ and $nx = 4$ using the full aerodynamic eigenmode model. The solid line indicates the result for the transverse displacement w, and the dashed line indicates the result for the in-plane motion u and v. It is found that the LCO frequency for both transverse w and in-plane u and v displacements increases as the flow velocity increases.

The trend with aspect ratio $AR \equiv L/c = 0.75$, 1.0, 1.5, and 3.5 and $ny = 2$ and $nx = 4$ using the reduced-order aerodynamic model with $R_a = 7$ is shown in Fig. 14. It is expected that the growth rate of

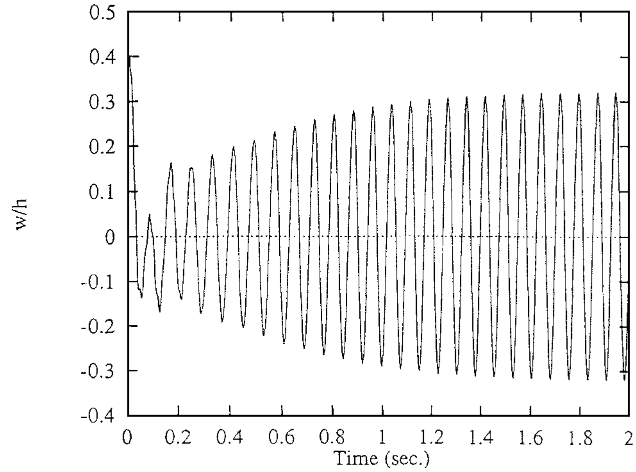

a) Nondimensional transverse deflection

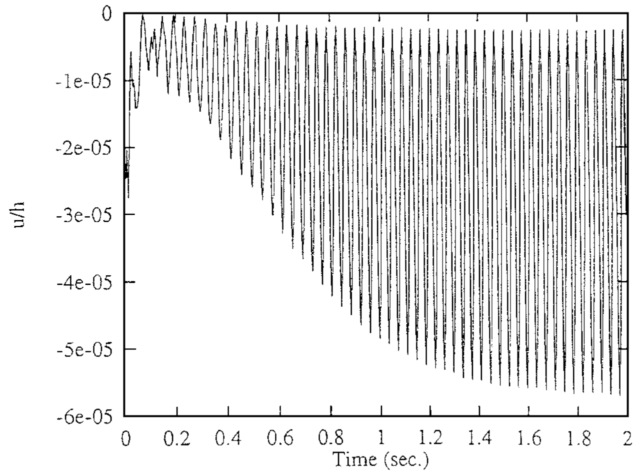

b) In-plane displacement in x direction

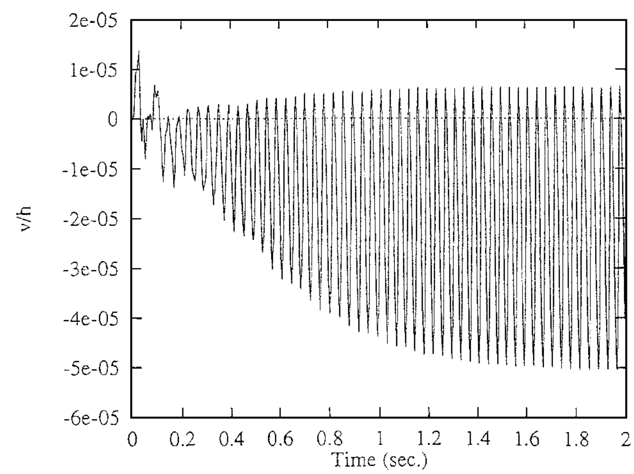

c) In-plane displacement in y direction

Fig. 9 LCO for $U = 45$ m/s.

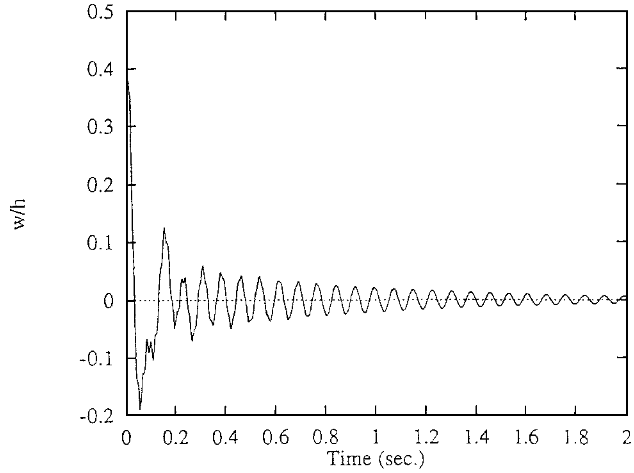

Fig. 10 Decaying oscillation of the nondimensional transverse response for $U = 40$ m/s.

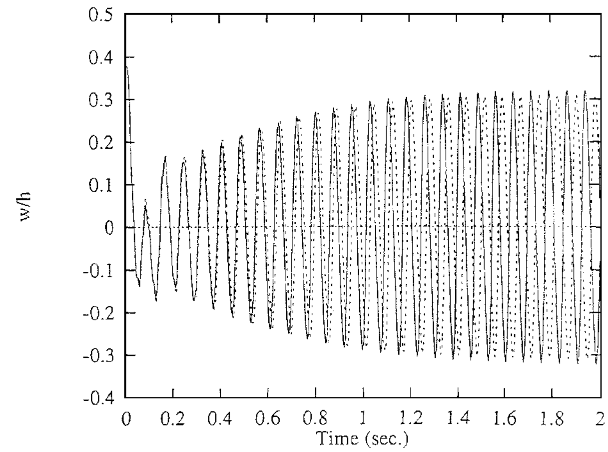

Fig. 11 Comparison of LCO for $U = 45$ m/s from ——, the full aerodynamic eigenmodes, and - - -, the reduced-order model with $R_a = 7$.

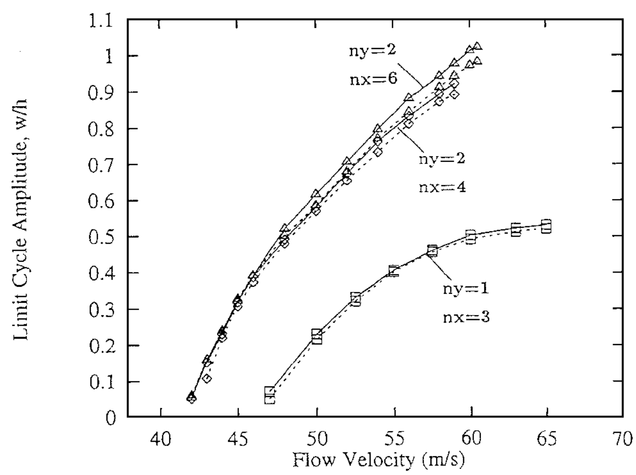

Fig. 12 Limit cycle amplitudes vs flow velocity U for aspect ratio $L/c = 1$, $ny = 1$, $nx = 3$, $ny = 2$, $nx = 4$, and $ny = 2$ and $nx = 6$ from ——, the full aerodynamic eigenmodes, and - - -, the reduced-order model with $R_a = 7$.

the limit cycle amplitude with flow velocity increases as the aspect ratio of the plate increases for large aspect ratios. This is physically true because the wing behaves more like a beam and less like a plate as the aspect ratio increases sufficiently. However, for the range of aspect ratios shown in Fig. 14, the limit cycle response is on the order of the plate thickness well beyond the linear flutter velocity.

When we calculated the LCO using both full- and reduced-order aerodynamic models, we found that there is a numerical instability (numerical divergence) at higher flow velocity for larger Δx (Δt) or smaller km. For example, when $km = 10$ the numerical divergence will occur when $U > 54.5$ m/s for $AR \equiv L/c = 1$ and $ny = 2$ and $nx = 4$. To obtain the LCO in the higher-flow-velocity range, we have to increase km and the corresponding kmm, e.g., we used $km = 20$ and $kmm = 80$ in Fig. 12 for $ny = 2$ and $nx = 4$ and $ny = 2$ and $nx = 6$. This is because, as shown in Fig. 13, the LCO frequency rapidly increases in the higher-flow-velocity range. Especially, for the higher in-plane displacement oscillation frequency, it is necessary to have a very small time step Δt to maintain numerical stability. Typically, more than 75 points per cycle are sufficient for the numerical stability. The reduced-order aerodynamic model has

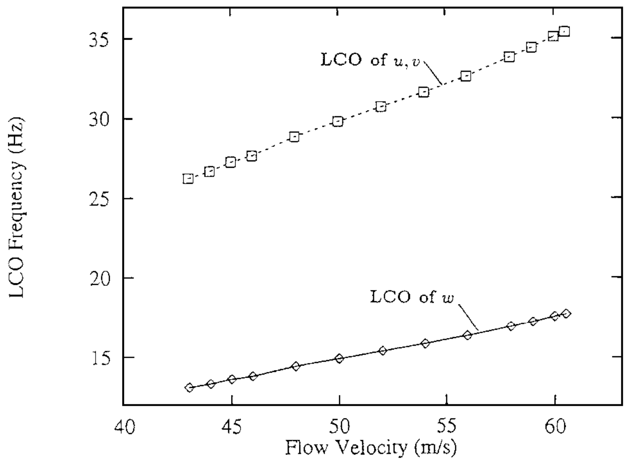

Fig. 13 LCO frequency vs flow velocity U for aspect ratio $L/c = 1$, $ny = 2$, and $nx = 4$ from ——, w motion, and - - -, u and v motions.

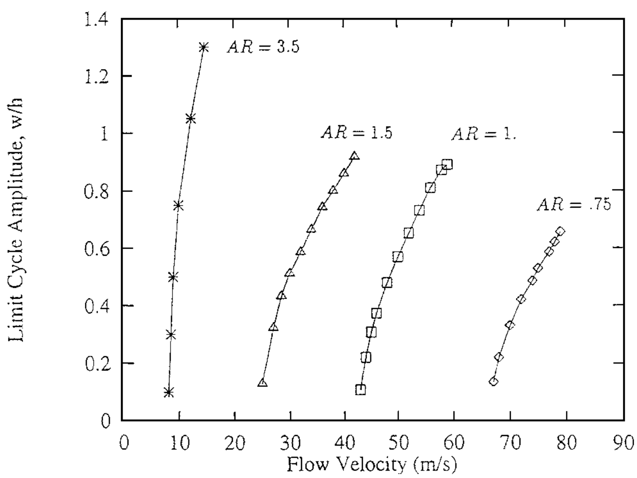

Fig. 14 Limit cycle amplitudes vs flow velocity U for several aspect ratio calculated from reduced-order model with $R_a = 7$.

a special advantage in saving computational time when the larger km and kmm are used, in that the time step needed for numerical stability of the time-marching scheme does not require the spatial discretization to be made smaller as is true when using the vortex lattice model directly in the aeroelastic analysis. We conclude this discussion by noting the correspondence of our theoretical results with the experimental results of Doggett and Soistmann.[7] First we quote these authors on their observations:

> A few comments about the nature of the flutter that was observed are in order. For the lower sweep angles flutter onset was clear in that at flutter the response began to increase at a rapid rate in the usual divergent amplitude oscillation. As sweep angle was increased, however, the onset of flutter became less distinct. As the flutter condition was approached the higher sweep models exhibited long bursts of lowly damped oscillations. The flutter condition itself was in the nature of a limited amplitude oscillation.

These authors tested delta (triangular) wings with the lower sweep angles corresponding to higher aspect ratios and the higher sweep angles corresponding to lower aspect ratios. For the latter they observed "limited amplitude oscillations," as we have found here for low-aspect-ratio wings. Recently completed calculations by the present authors for delta wings (to be reported separately) have further confirmed these results.

Concluding Remarks

Vortex lattice aerodynamic theory has been used to construct a reduced-order aerodynamic model that has been successfully applied to determine the nonlinear limit cycle response of a cantilever plate model of a wing with a geometric structural nonlinearity. It was shown that the unsteady three-dimensional flow can be modeled accurately using a few aerodynamic eigenmodes plus a static correction technique and, thus, can be easily coupled to a structural system for nonlinear aeroelastic analysis. The present method has good accuracy and computational efficiency for both linear flutter and nonlinear response analysis.

The present paper provides new insight into a nonlinear aeroelastic phenomenon not previously widely appreciated, i.e., LCO for low-aspect-ratio wings that have a plate-like structural behavior. This adds to our understanding of nonlinear aeroelastic wing theory.

Whereas a simple rectangular wing-plate geometry is considered here, wings of general planform can be treated similarly by first finding the linear structural eigenmodes of the wing using a finite element code, for example.

Acknowledgments

This work was supported under Air Force Office of Scientific Research Grant "Limit Cycle Oscillations and Nonlinear Aeroelastic Wing Response" and NASA Langley Research Center Grant "Flutter of Wing and Control Surface with Freeplay." C. I. Chang and Brian Sanders and Donald Keller are the respective Grant Monitors. All numerical calculations were done on a T916 supercomputer in the North Carolina Supercomputing Center.

References

[1] Dowell, E. H., *Aeroelasticity of Plates and Shells*, Kluwer, Dordrecht, The Netherlands, 1975, pp. 35–49.

[2] Ricketts, R. H., Noll, T. E., Whitlow, W., Jr., and Huttsell, L. J., "An Overview of Aeroelasticity Studies for the National Aerospace Plane," *Proceedings of the AIAA/ASME/ASCE/AHS/ASC 34th Structures, Structural Dynamics, and Materials Conference*, AIAA, Washington, DC, 1993, pp. 152–162.

[3] Hopkins, M. A., and Dowell, E. H., "Limited Amplitude Panel Flutter with a Temperature Differential," *Proceedings of the AIAA/ASME/ASCE/AHS/ACS 35th Structures, Structural Dynamics, and Materials Conference*, AIAA, Washington, DC, 1994, pp. 1343–1355.

[4] Weiliang, Y., and Dowell, E. H., "Limit Cycle Oscillation of a Fluttering Cantilever Plate," *AIAA Journal*, Vol. 29, No. 11, 1991, pp. 1929–1936.

[5] Hall, K. C., "Eigenanalysis of Unsteady Flows About Airfoils, Cascades, and Wings," *AIAA Journal*, Vol. 32, No. 12, 1994, pp. 2426–2432.

[6] Dowell, E. H., "Eigenmode Analysis in Unsteady Aerodynamics: Reduced-Order Models," *AIAA Journal*, Vol. 34, No. 8, 1996, pp. 1578–1588.

[7] Doggett, R. V., and Soistmann, D. L., "Some Low-Speed Flutter Characteristics of Simple Low-Aspect-Ratio Delta Wing Models," NASA TM-101547, Jan. 1989.

[8] Florea, R., and Hall, K. C., "Reduced Order Modeling of Unsteady Flows About Airfoils," *Aeroelasticity and Fluid Structure Interaction Problems*, edited by P. P. Friedmann and J. C. I. Chang, AD-Vol. 44, American Society of Mechanical Engineers, New York, 1994, pp. 49–68.

A. Chattopadhyay
Associate Editor